

ChemSusChem

Supporting Information

Stable Na⁺ Ion Storage via Dual Active Sites Utilization in Covalent Organic Framework-Carbon Nanotube Composite

Anupam Dey, Atin Pramanik, Sougat Purohit, Sandip Biswas, Shreyasi Chattopadhyay, Tymofii S. Pieshkov, Gopalakrishnan Sai Gautam, Pulickel M. Ajayan,* and Tapas Kumar Maji*

Supporting Information

Stable Na⁺ Ion Storage via Dual Active Sites Utilization in Covalent Organic Framework-Carbon Nanotube Composite

Anupam Dey,^{1#} Atin Pramanik,^{2#} Sougat Purohit,³ Sandip Biswas,¹ Shreyasi Chattopadhyay,² Tymofii S. Pieshkov,^{2,4} Gopalakrishnan SaiGautam,³ Pulickel M. Ajayan,^{2} Tapas Kumar Maji^{1*}*

¹Chemistry and Physics of Materials Unit, School of Advanced Materials, International Centre for Materials Science, Jawaharlal Nehru Centre for Advanced Scientific Research, Jakkur, Bangalore -560064, India

²Department of Materials Science and NanoEngineering, Rice University, Houston, Texas-77005, United States

³Department of Materials Engineering Indian Institute of Science, Bengaluru-560012, India

⁴Applied Physics Graduate Program, Smalley-Curl Institute, Rice University, Houston, TX, 77005 United States.

[#]Contributed equally.

Experimental procedure:

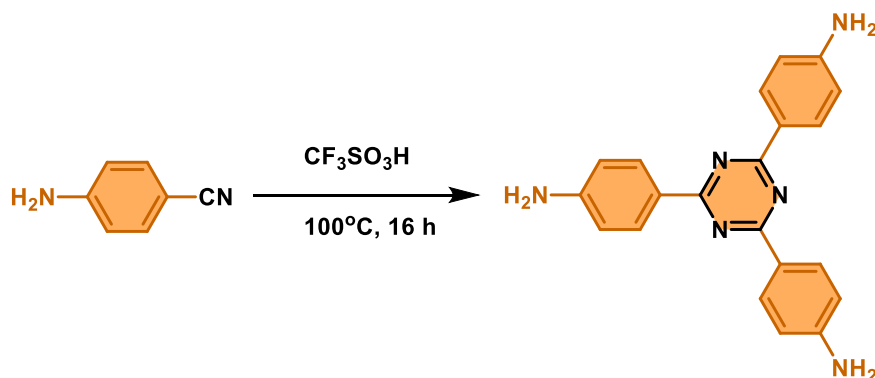
Materials:

4-aminobenzonitrile and trifluoromethanesulfonic acid were purchased from Sigma-Aldrich Chemical Co. Ltd. KOH have brought from Thomas Baker (Chemicals) Pvt. Ltd. Pyromellitic dianhydride (PMDA), m-cresol and isoquinoline have purchased form Spectrochem Pvt. Ltd. Amino functionalized multiwall carbon nanotube (MWCNT-NH₂) was purchased from Platonic nanotech Pvt. Ltd. NMR solvent, DMSO-d₆ was purchased from Sigma Aldrich Chemical Co. Ltd.

Synthesis:

1. Synthesis of 4,4',4''-(1,3,5-triazine-2,4,6-triyl)trianiline (TAPTz):

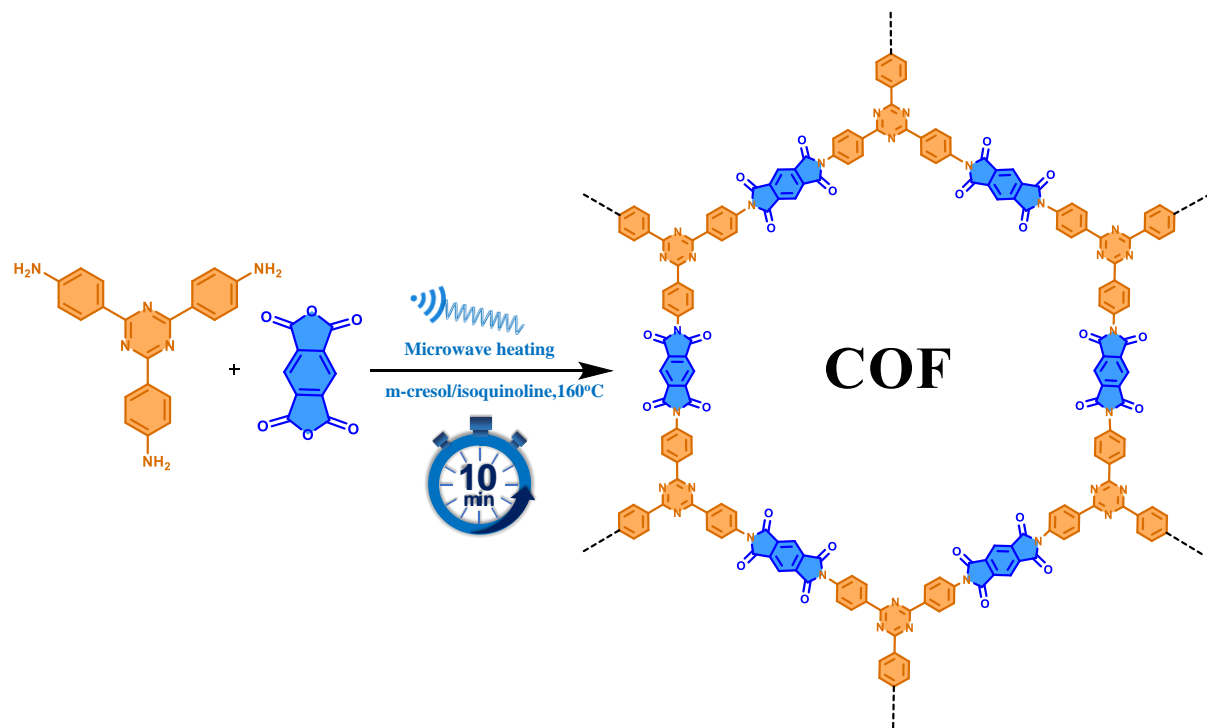
By following earlier report TAPTz was synthesized from 4-aminobenzonitrile.¹ Briefly, in a 50 mL Schlenk tube, 1.18 g (10 mmol) of 4-aminobenzonitrile was taken in inert atmosphere at 0 °C. Then, 3.6 mL (40.0 mmol) of trifluoromethanesulfonic acid was added dropwise to that. Next, the reaction mixture was heated under inert atmosphere at 110 °C for 16 h with condenser and constant stirring. After cooled down to room temperature, 50 mL distilled water was added to the mixture, and followed by 4 M NaOH solution until the pH reaches to 7. The light yellow coloured precipitate was filtered and washed with copious amount of distilled water. Finally, pure yellow product was obtained after column chromatography (hexane/ethyl acetate; from 1:1 to 1:10). The purity of TAPTz was confirmed by liquid state ¹H and ¹³C NMR study. **¹H NMR (600 MHz, DMSO-d₆)** δ 8.34 (d, *J* = 8.7 Hz, 6H), 6.69 (d, *J* = 8.7 Hz, 6H), 5.90 (s, 6H) (Figure S1). **¹³C NMR (151 MHz, DMSO-d₆)** δ 169.55, 152.95, 130.12, 122.91, 113.08 (Figure S2).



Scheme S1. Synthesis of 4,4',4''-(1,3,5-triazine-2,4,6-triyl)trianiline (TAPTz).

2. Synthesis of COF:

Microwave assisted COF synthesis was performed according to previous report from our group.² At first, two building units, i.e. TAPtZ (17.7 mg, 0.05 mmol) and PMDA (16.4 mg, 0.075 mmol) were weighted in a 10 mL glass microwave tube (G-10). Then, m-cresol (2 mL)/ isoquinoline (0.1 mL) were added to it and capped by a septum. After sonication for 5 minutes the tube was inserted into Anton Paar microwave synthesis reactor (monowave 200) and heated at 160 °C by microwave irradiation with 10 min hold time. After the completing the holding time it was cooled down to room temperature. A yellow precipitate was collected by washing with THF (20 mL). Further, the solid precipitate was soxhled in THF for 24 h and dried under vacuum at 70 °C to afford pure, highly crystalline **COF** (25.1 mg, 74% yield).

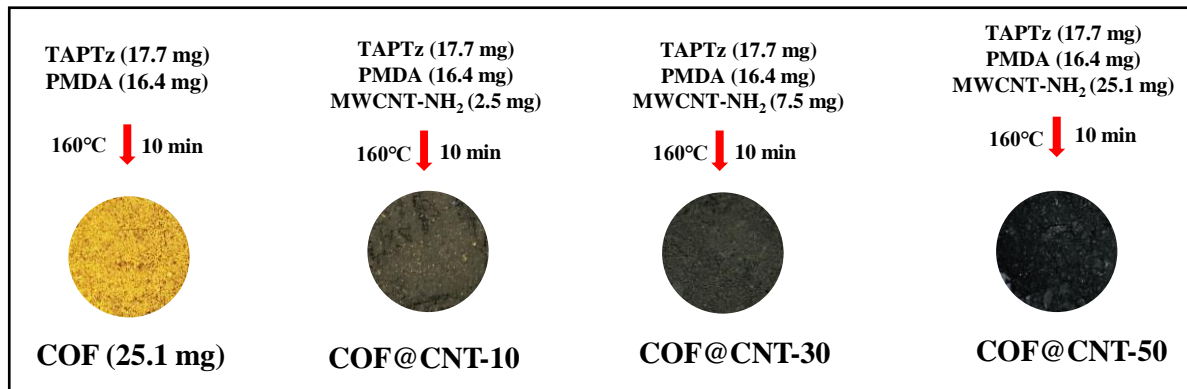


Scheme S2. Synthesis of COF via microwave irradiation for 10 min.

3. Synthesis of COF@CNT-X nanocomposites:

The **COF@CNT-X** (X= 10, 30, 50 wt%) nanocomposites were synthesised by following the similar synthesis method of **COF** with the addition of amino functionalized multiwall carbon nanotube (MWCNT-NH₂) before polymerization. The mass content of MWCNT-NH₂ in the composites were controlled as 10 wt%, 30 wt%, and 50 wt% based on the amount yield of pristine COF. Briefly, 17.7 mg (0.05 mmol) of TAPtZ, 16.4 mg (0.075 mmol) of PMDA and appropriate weight of MWCNT-NH₂ were dispersed into a 10 mL glass microwave vial and

charged with the solution of m-cresol/ isoquinoline (2 mL/0.10 mL). The mixture was sonicated for 10-15 min and heated at 160°C by microwave radiation for 10 min in the Anton Paar microwave synthesis reactor (monowave 200). After cooling, the precipitate was collected by filtration and washed with copious amounts of anhydrous THF. Finally, pure **COF@CNT-X** nanocomposites were obtained after soxhlation in THF for 24 h and followed by vacuum dry at 70 °C. For **COF@CNT-X** nanocomposites, the MWCNT-NH₂ amounts are as follows: 2.5 mg (for 10 wt%), 7.5 mg (for 30 wt%), 25.1 mg (for 50 wt%).



Scheme S3. Synthesis of **COF@CNT-X** (X= 10, 30, 50) nanocomposites.

4. Synthesis of PMDA-CNT model compound:

PMDA-CNT model compound was synthesized by following similar microwave pathway by taking PMDA monomer and NH₂-MWCNT in a G-10 microwave vial. Then m-cresol/isoquinoline was added into it and mixture was heated at 160°C for 10 minutes.

General characterization techniques:

Liquid state ¹H-NMR spectra were recorded on a Bruker AVANCE-400 NMR spectrometer operating at frequency of 400 MHz. The chemical shifts recorded as ppm, and all spectra were calibrated against TMS. Powder X-ray diffraction (PXRD) patterns were measured in Rigaku Smart Lab SE instrument using Cu-K_α radiation ($\lambda = 1.5406 \text{ \AA}$). Thermogravimetric analysis were carried out by Mettler Toledo-TGA 850 instrument in N₂ atmosphere within the temperature range 30 - 800 °C at a heating rate of 5 °C/min. N₂ sorption isotherm at 77 K and CO₂ sorption isotherm at 298K were measured in QUANTACHROME instruments Autosorb iQ₂. Before performing sorption isotherm measurements, samples were degassed at 180 °C and $1 \times 10^{-1} \text{ Pa}$ vacuum for 18 h. Further, Pore size distributions were obtained from the adsorption data by fitting a nonlocal density functional theory (NLDFT) model. ¹³C-Solid state cross-polarization magnetic angle spinning (CP/MAS) NMR spectrum was measured in a Varian

infinity plus 300WB spectrometer. FTIR spectra were recorded in Bruker FT-IR spectrometer in ATR mode. Solid state UV-Vis studies were performed in solid state using Agilent Cary series UV-Vis-NIR spectrophotometer instrument. Field Emission Scanning Electron Microscope (FE-SEM) images were recorded by Bruker Leica-S440I FESEM instrument. Samples were prepared by dispersing the samples in ethanol homogeneously and drop casted on a silicon wafers. The FESEM images were collected by placing the silicon wafer under high vacuum with an accelerating voltage of 100 kV. Energy dispersive spectroscopy (EDS) analysis was performed with an EDAX genesis instrument attached to the FESEM column. Transmission Electron Microscopic (TEM) images were collected by using JEOL JEM-3010 TEM with an accelerating voltage of 200 kV. The samples were dispersed in ethanol and drop-casted over carbon-coated copper grid prior to TEM analysis.

Electrochemical characterization:

The performance of sodium-ion batteries was assessed by fabricating 2032-type coin cells (MTI-USA) within a glovebox environment. The protocol for preparing the working electrodes was followed meticulously by employing the conventional slurry casting technique. The slurry composition consisted of active materials, super-P carbon (conductive carbon), and a blend of sodium carboxymethyl cellulose (CMC) with styrene-butadiene rubber (SBR) binder, mixed in de-ionized water solvent using a mixer (Thinky) at a weight ratio of 75:15:10. The resulting homogeneous slurry ink was uniformly coated onto aluminium foil sheets with a thickness of 15 μ m. Subsequently, the coated aluminium sheets underwent a 12-hour drying process at 80 °C in a vacuum oven. Calendering was performed on the dried coated aluminium foil at a rate of 4.0 tons per square inch, shaping the electrodes into disks with a diameter of 12.5 mm. The loading of active material mass was approximately \sim 2.0 mg cm⁻². The assembly of the coin cells took place within the glovebox, with the interior environment filled with Ar (M'BRAUN, Germany) to maintain moisture and oxygen levels below 0.5 ppm. Shiny sodium metal was used to construct the SIB half-cells, serving as the counter and reference electrodes. At the same time, Celgard 2300 was employed as the separator, and the electrolyte comprised 1.0 M NaPF₆ in diglyme (Thermo Fisher Scientific, purity 99+%). After assembly, cyclic voltammetry (CV) measurements were conducted using a galvanostat-potentiostat (PGSTAT30, Autolab, The Netherlands) across various scan rates ranging from 0.1 to 1.0 mV s⁻¹. Galvanostatic charge-discharge (GCD) studies were performed using a LAND CT2001A battery tester at different current densities. The SIB half-cells underwent testing within a 1.3-3.5 V voltage window for CV and GCD measurements.

***Ex situ* XPS measurements:**

After fifteen charge/discharge cycles, the SIB cells were halted. The first cell was stopped at full charge (3.5 V), and the second cell was stopped at full discharge (1.3 V). Subsequently, the cells were promptly opened within the glovebox, and the electrodes were thoroughly cleaned with DMC. The charged and discharged electrodes underwent ex-situ XPS analysis to elucidate the electrochemical mechanism, utilizing the PHI Quantera SXM scanning X-ray microprobe equipped with a 1486.6 eV monochromatic Al $\text{K}\alpha$ X-ray source.

Structural Modelling of COF:

Materials Studio 2020 package software was used to model the COF's structure. The space group with the highest degree of symmetry was employed in the modelling. The lattice models were optimized by using the MS Forcite molecular dynamics module (Universal force fields). Next, using the Reflex module, structural refinement were done use the Pawley method. Berar-Baldinozzi technique with pseudo-Voigt peak profiles was used to correct for peak asymmetry. On the basis of earlier research, the unit cell parameters a , b , crystallite size along a , b , and c , FWHM parameters, U , V , and W , profile parameters N_A and N_B , and zero-point were improved. Polynomials of 20th order were used to refine the background.³⁻⁶

Density Functional Theory (DFT) Calculations:

We used the Vienna ab initio simulation package (VASP)^{7, 8} for all the DFT calculations, utilizing plane-wave basis sets (cut-off energy of 520 eV), projected augmented wave (PAW)⁹ potentials (namely Na 08Apr2002, H 15Jun2001, C 08Apr2002, N 08Apr2002 and O 08Apr2002) and the strongly constrained and appropriately normed (SCAN)¹⁰ exchange-correlation functional. We obtained the energy of each structure following non-symmetry-preserved structure relaxation, using Γ -centred k -points with a mesh density of 32 per Å, an energy convergence criterion of 10^{-5} eV, and an atomic force convergence criterion of 0.03 eV Å⁻¹. We allowed the atomic positions, cell shape, and cell volume to change during each structure relaxation.

First, we relaxed the experimentally obtained PXRD structure of the **COF**, yielding unit cell parameters of $a = b = 35.96$ Å, $c = 3.67$ Å, $\alpha = \beta = 90^\circ$, and $\gamma = 120^\circ$ (Figure S15), which closely agreed with the experimental cell parameters ($a = b = 36.82$ Å, $c = 3.56$ Å; $\alpha = \beta = 90^\circ$, $\gamma = 120^\circ$). We adopted a sequential approach to determine the Na^+ arrangement in the **COF** during sodiation, by adding Na -ions to the unit cell one by one. For each Na^+ added, we

determined the lowest energy relaxed configuration of the **COF** and then added the next Na^+ to this lowest energy configuration. For instance, for the first Na^+ addition to the **COF** unit cell, we needed to examine whether Na^+ binds favourably to pyromellitic or triazine units, which amounts to considering a maximum of 18 configurations, corresponding to the single occupation of each 18 Na^+ sites per **COF** unit cell (Figure S15a). We used the pymatgen package¹¹ to enumerate all possible symmetrically distinct Na configurations, namely two structures (i.e., one each with Na adjacent to one triazine unit and one pyromellitic unit), relaxed both configurations (Figure S16).

Following our sequential approach, we enumerated symmetrically distinct sites to which an additional Na can be added to the ground state structure at Na_1COF to obtain the ground state configuration at Na_2COF . Subsequently, we repeated this sequential approach for Na contents till Na_8COF to identify the ground state Na configuration at each sodiated **COF** composition (Figure S18, S19). This approach relies on the assumption that every Na^+ added to the **COF** influences the site that a subsequent Na will bind to, i.e., Na-migration within a single **COF** ring becomes less facile once Na binds to a site. Once we obtained the energies of different Na configurations and compositions within the **COF** unit cell, we used the pymatgen package to construct the pseudo-binary convex hull.

For getting the ground state Na_{12}COF configuration (Figure S20b), we added 4 Na simultaneously to the ground state Na_8COF configuration. Note that adding 4 Na atoms simultaneously yielded 210 total structures, out of which we chose only 20 structures with the lowest electrostatic energies for further calculations with DFT, as calculated using the Ewald summation technique,¹² to minimize computational costs associated with DFT. For the Ewald calculation, we assigned charges of +1, +1, -2, -3 and 0 for Na, H, O, N and C respectively. Note that with all other compositions of Na_xCOF , we added just one Na, which yields significantly fewer enumerated structures, enabling us to perform DFT calculations on all the structures.

We calculated the average Na-intercalation voltage, referenced to the Na/Na^+ electrode, as a function of Na content in the COF electrode, using the following equation:

$$V = - \frac{E(\phi_1) - E(\phi_2) - E(\text{Na})}{F(n_{\text{Na}}^{\phi_1} - n_{\text{Na}}^{\phi_2})}$$

Where, $E(\phi_i)$ and $E(Na)$ are the DFT calculated energies per formula unit of phase ϕ_i and bulk Na respectively, $n_{Na}^{\phi_i}$ is the number of Na per formula unit of phase ϕ_i and F is the Faraday's constant. Note that our voltage calculations neglect any entropic and pressure-volume contributions.

Supplementary figures:

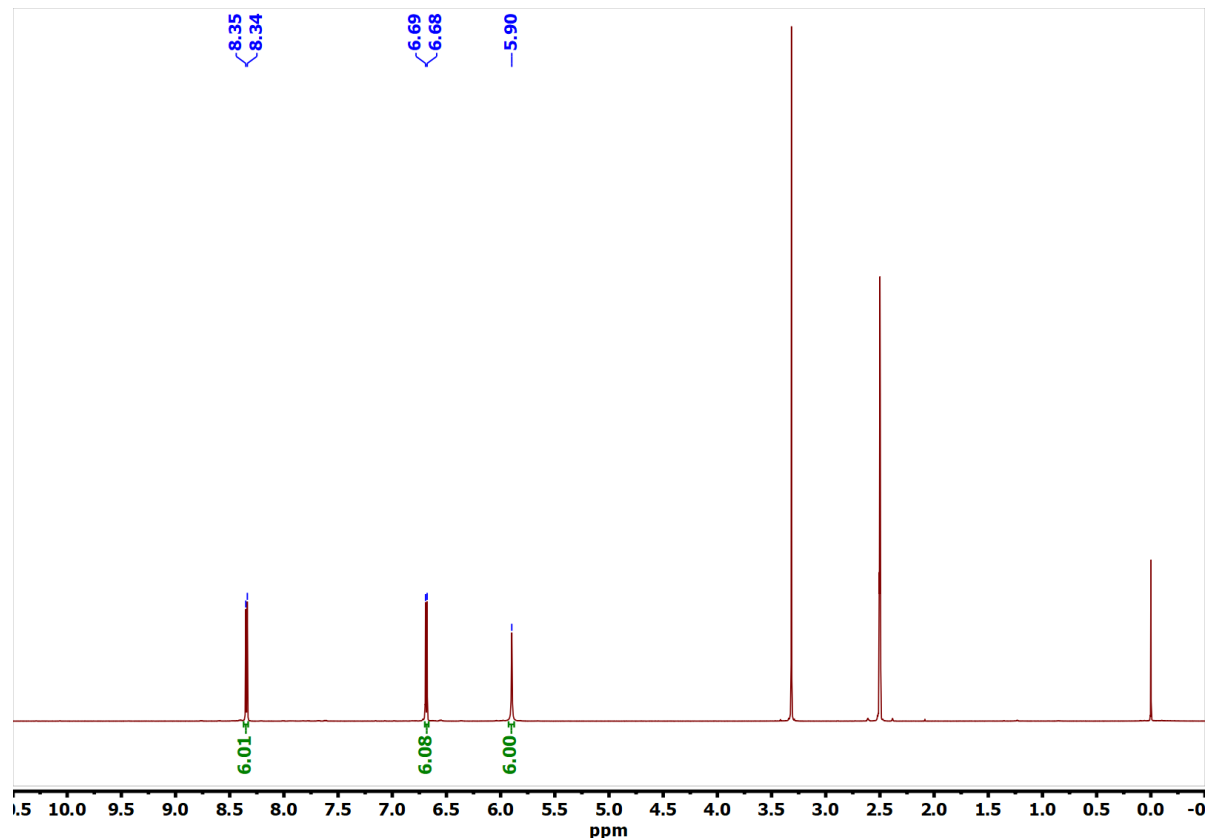


Figure S1. ${}^1\text{H}$ -NMR spectrum of TAPTz monomer.

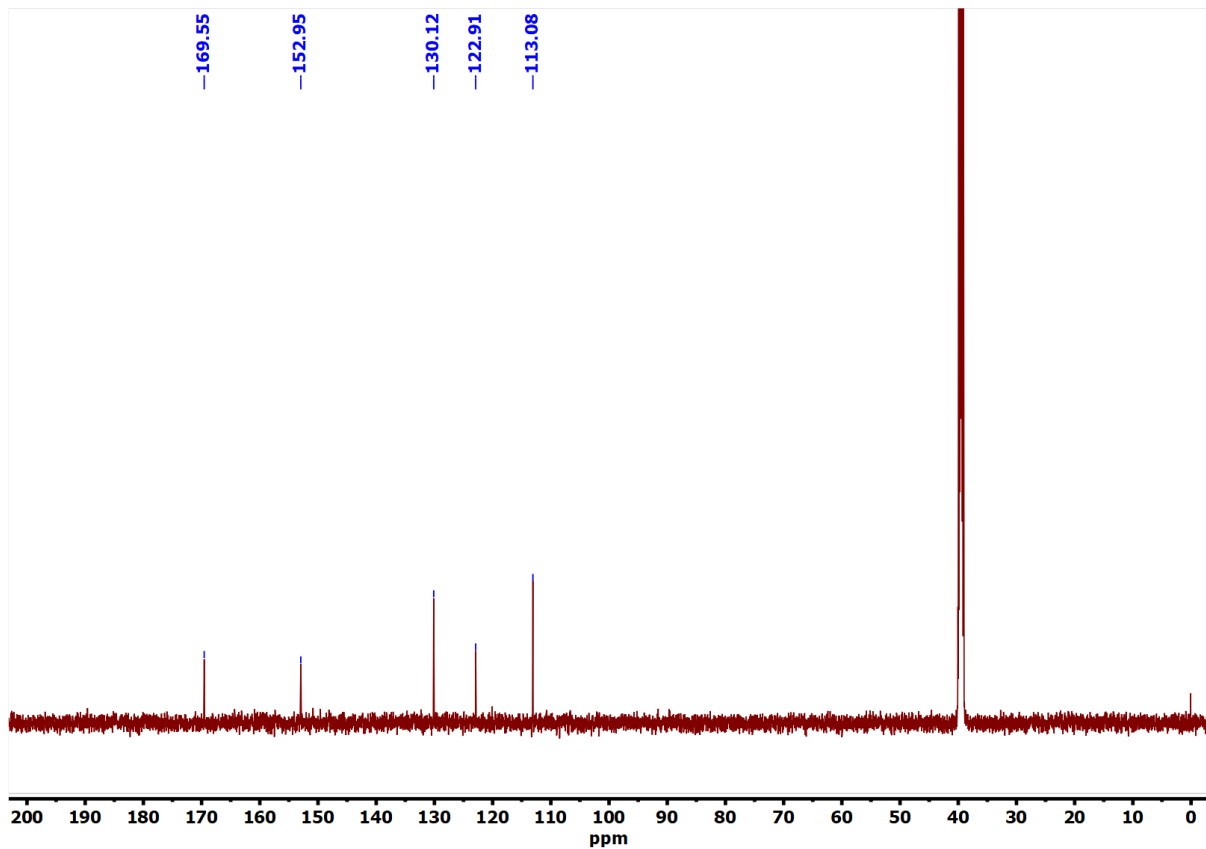


Figure S2. ¹³C-NMR spectrum of TAPTz monomer.

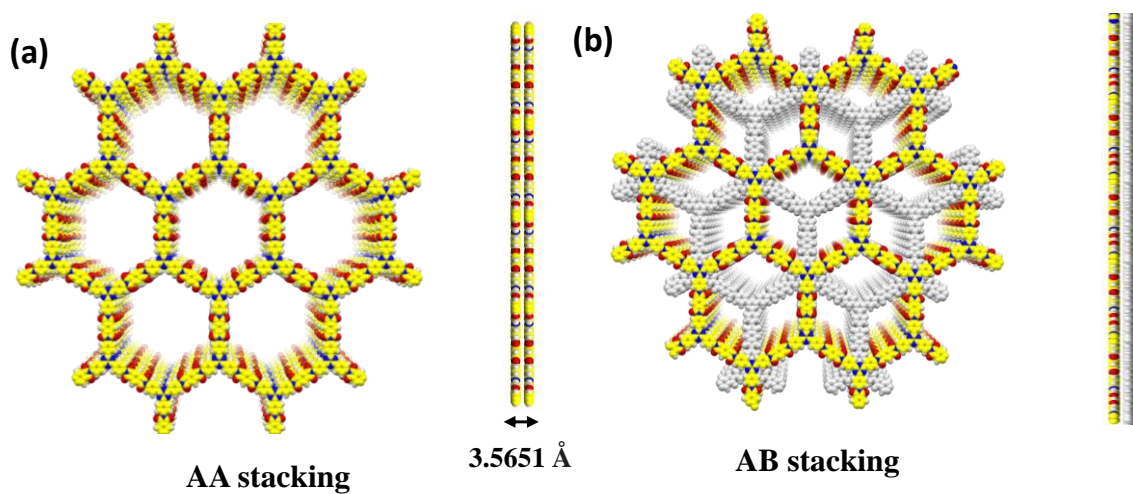


Figure S3. Model structure of COF for (a) AA stacking (eclipsed); along the crystallographic 'c' axis (left) and along the crystallographic 'b' axis (right). (b) AB stacking (eclipsed); along the crystallographic 'c' axis (left) and along the crystallographic 'b' axis (right).

Table S1. Fractional atomic coordinates of the unit cell for **COF** by using *P6/mmm* space group (AA stacking).

Space group = P6/mmm (hexagonal)
a=b=36.823,c= 3.565; $\alpha=\beta=90^\circ$, $\gamma=120^\circ$

Atom	x	y	z
C	0.64471	0.35529	0
N	0.68865	0.31135	0
C	0.62051	0.24102	0
C	0.57676	0.15351	0
N	0.55373	0.10746	0
C	0.64252	0.21914	0
C	0.62065	0.1754	0
H	0.67701	0.2364	0
H	0.6379	0.15815	0
C	0.50716	0.07868	0
C	0.49871	0.03803	0
O	0.47806	0.08721	0
C	0.46098	0	0
H	0.43111	0	0

Table S2. Fractional atomic coordinates of the unit cell for **COF** by using $P6_3/mmc$ space group (AB stacking).

Space group = $P6_3/mmc$ (hexagonal)
 $a=b=36.823, c= 6.800; \alpha= \beta=90^\circ, \gamma=120^\circ$

Atom	x	y	z
C	0.97858	0.02142	3.25
N	1.02123	-0.02123	3.25
C	0.68809	0.31191	3.25
N	0.64543	0.35457	3.25
C	0.95525	-0.0895	3.25
C	0.91033	-0.17934	3.25
N	0.88725	-0.22549	3.25
C	0.71142	0.42284	3.25
C	0.75633	0.51267	3.25
N	0.77941	0.55883	3.25
C	0.97664	-0.11205	3.25
C	0.95476	-0.15594	3.25
H	1.01059	-0.09577	3.25
H	0.97388	-0.17036	3.25
C	0.84425	-0.25217	3.25
C	0.8333	-0.29603	3.25
O	0.81823	-0.24101	3.25
C	0.69003	0.44538	3.25
C	0.71191	0.48927	3.25
H	0.65607	0.42911	3.25
H	0.69279	0.50369	3.25
C	0.82242	0.5855	3.25
C	0.83337	0.62936	3.25
O	0.84843	0.57435	3.25
C	0.79438	-0.33333	3.25
H	0.76499	-0.33333	3.25

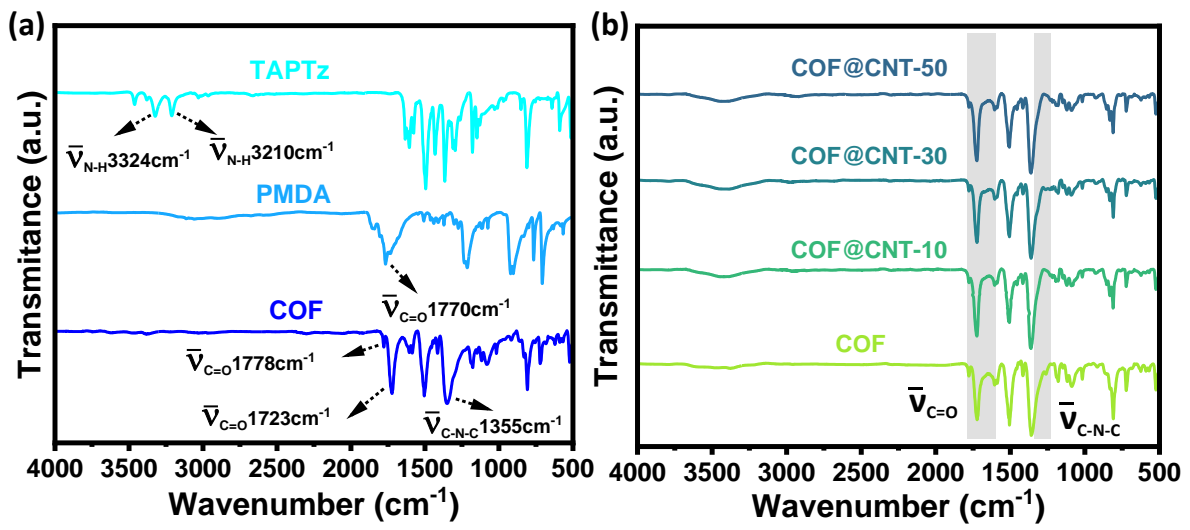


Figure S4. FTIR spectra of (a) COF along with the monomers, TAPTz and PMDA; (b) COF@CNT-X nanocomposites.

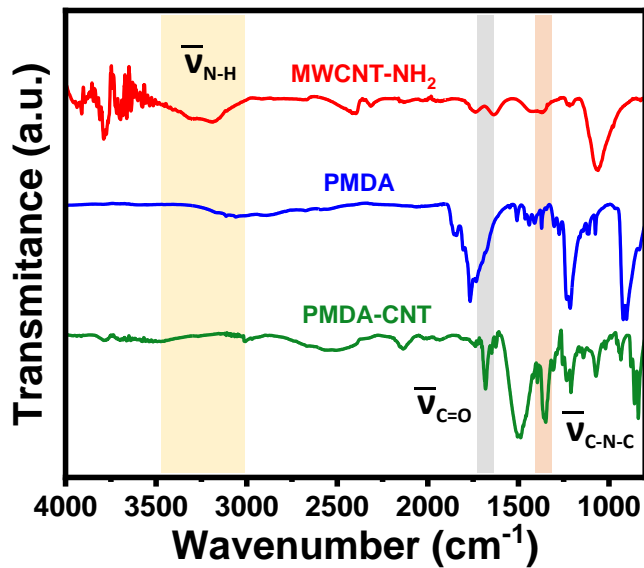


Figure S5. Calculated pore size distribution profile of COF and COF@CNT-X nanocomposites by non-local density functional theory (NLDFT) from N₂ sorption isotherms measured at 77K.

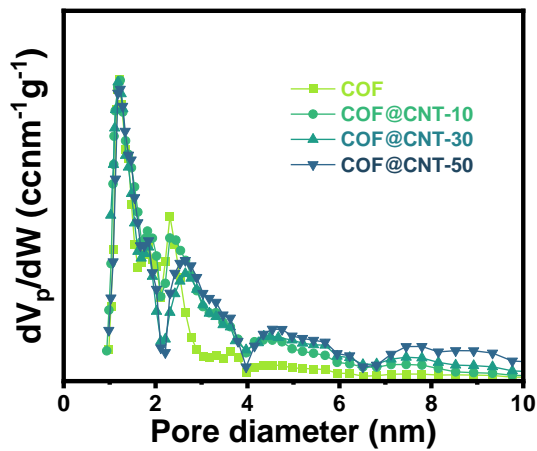


Figure S6. Calculated pore size distribution profile of **COF** and **COF@CNT-X** composites by non-local density functional theory (NLDFT) from N_2 sorption isotherms measured at 77K.

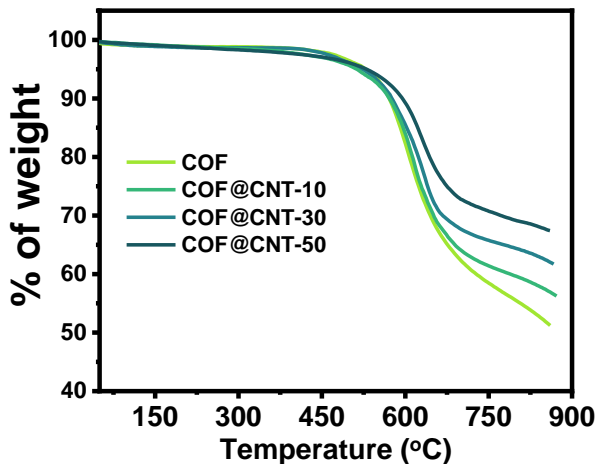


Figure S7. Thermogravimetric analysis (TGA) profile of **COF** and **COF@CNT-X** nanocomposites demonstrate the increased thermal stability after the composite formation.

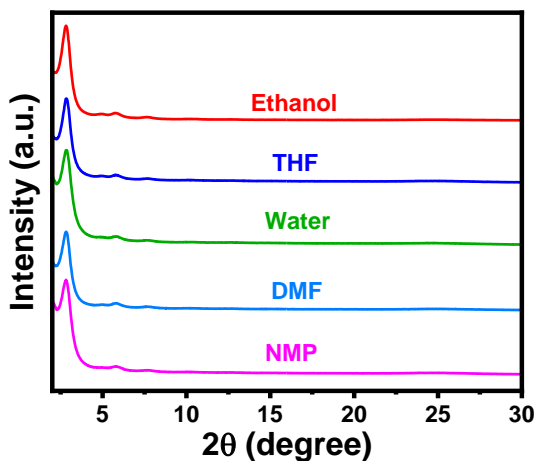


Figure S8. PXRD patterns recorded after soaking the **COF** into different organic solvents for 2 days.

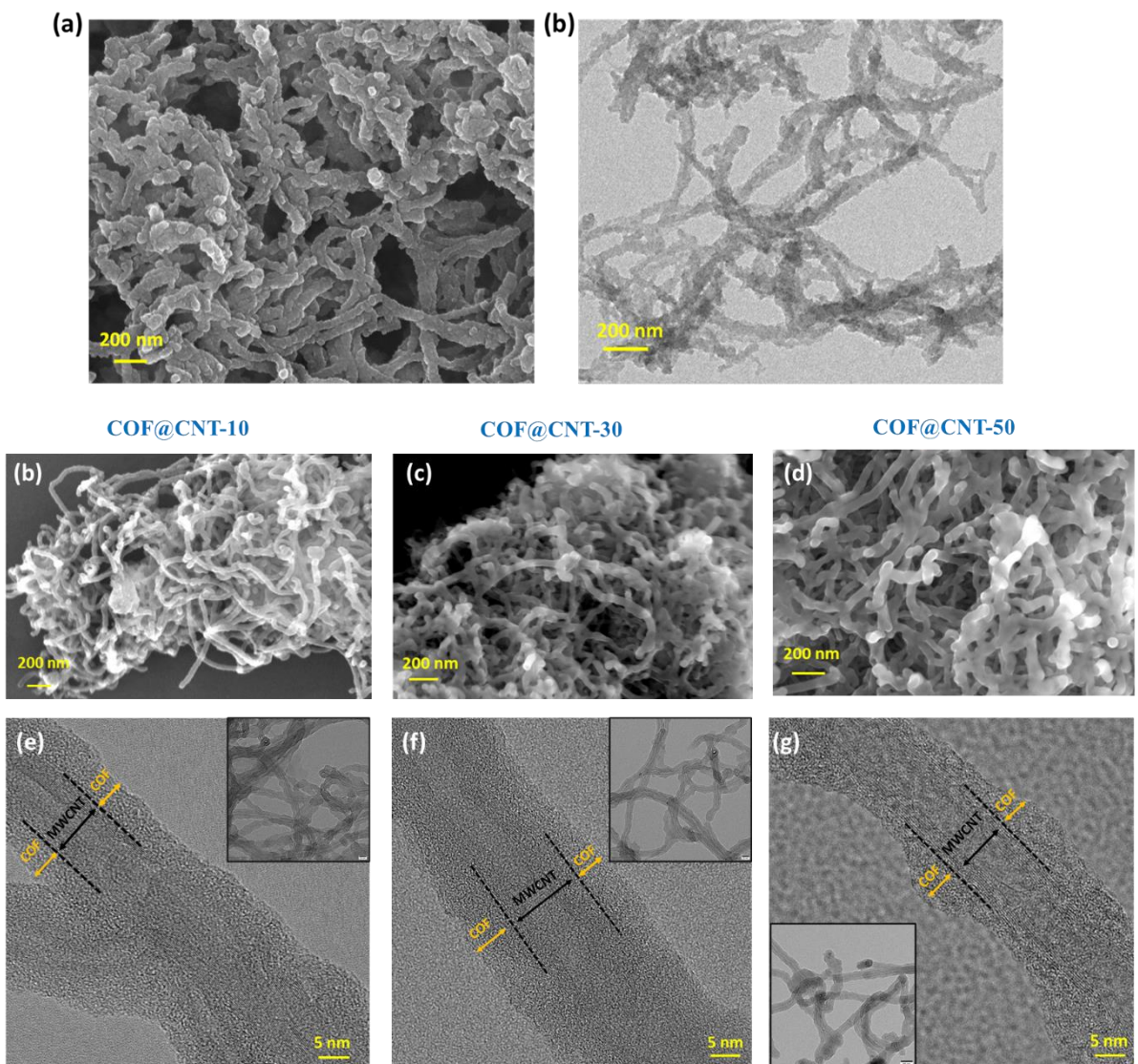


Figure S9. (a) FESEM and (b) TEM images of pristine COF. FESEM and HRTEM images of COF@CNT-X nanocomposites; (c)-(d) COF@CNT-10, (e)-(f) COF@CNT-30, (g)-(h) COF@CNT-50. Inset showing large scale TEM image for all the cases.

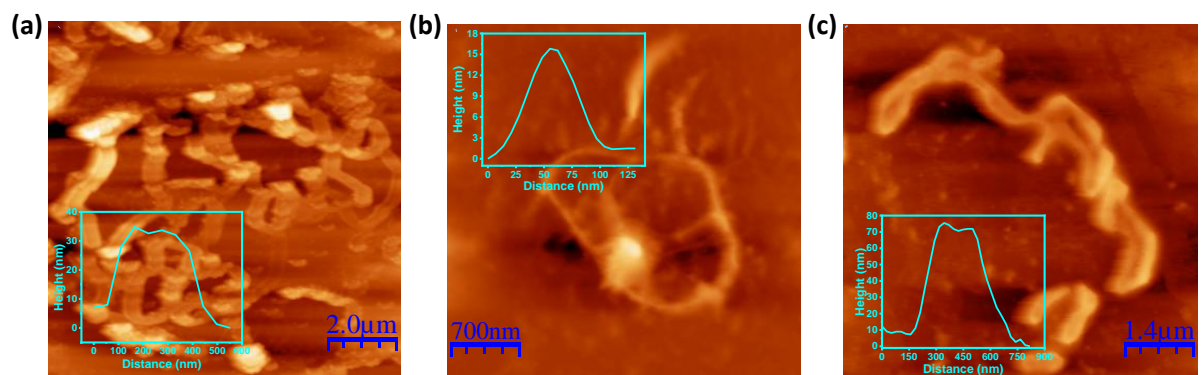


Figure S10. AFM image of (a) COF, (b) MWCNT-NH₂, and (c) COF@CNT50. Inset: corresponding height profile.

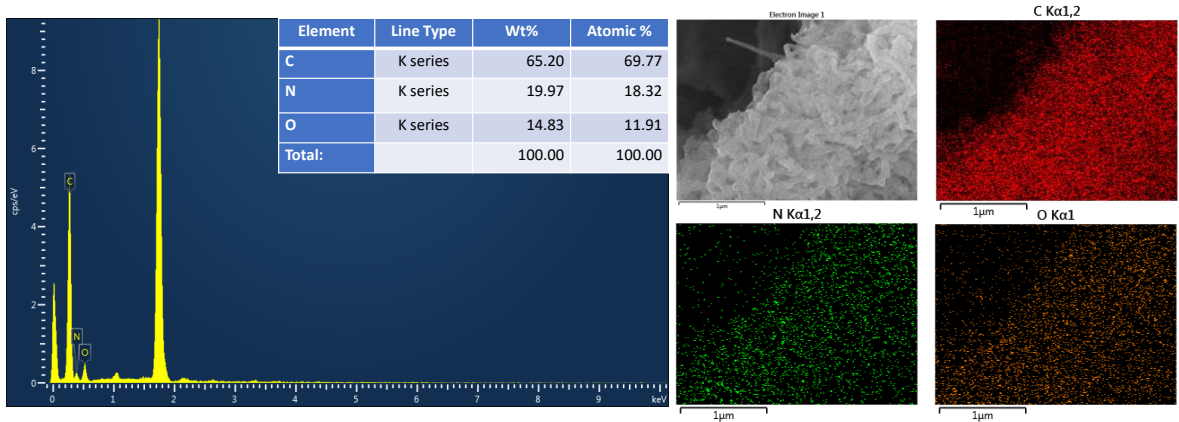


Figure S11. Energy dispersive X-ray analysis and elemental analysis of **COF@CNT-50** nanocomposite.

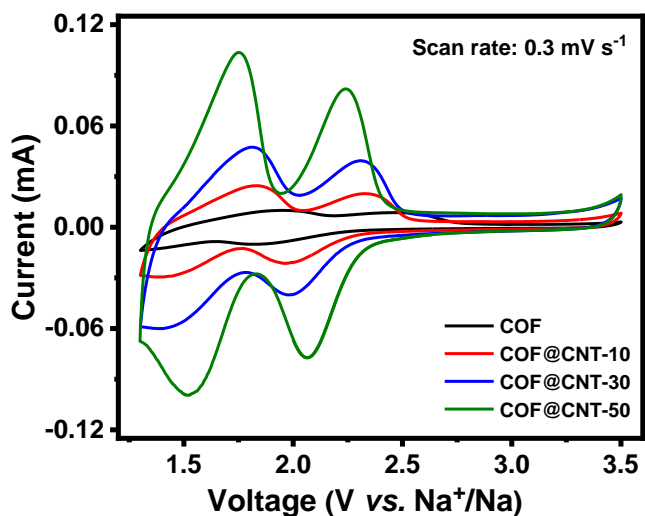


Figure S12. CV at 1.3-3.5 V voltage window at 0.3 mV s^{-1} scan rate for all four composites.

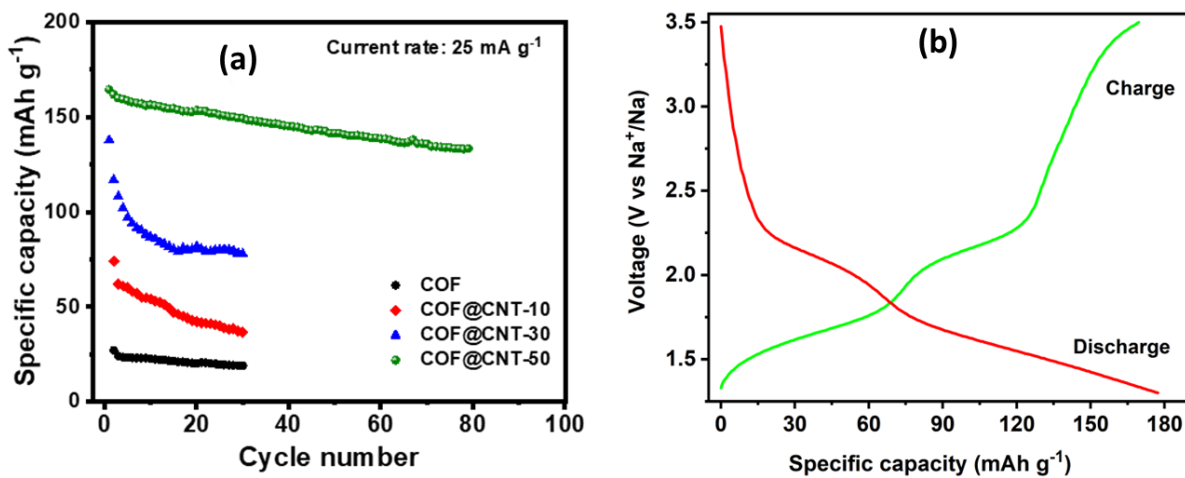


Figure S13. (a) Cycling performance of three composites and pristine COF materials at 1.3–3.5 V voltage window at 25 mA g⁻¹ current density. (b) The first cycle galvanostatic charge/discharge profile for the **COF@CNT-50** composition at 25 mA g⁻¹ current rate.

Calculation of theoretical capacity:

Theoretical capacity C_t (mAh g⁻¹) was calculated using the equation of

$$\begin{aligned}
 C_t (\text{mAh g}^{-1}) &= \frac{n \times F (\text{C mol}^{-1})}{M_{\text{unit}} (\text{g mol}^{-1})} \\
 &= \frac{n \times 96485 (\text{C})}{M_{\text{unit}} (\text{g})} = \frac{n \times 96485 (\text{A s})}{M_{\text{unit}} (\text{g})} \\
 &= \frac{n \times 96485 \times \frac{1000}{3600} (\text{mA h})}{M_{\text{unit}} (\text{g})} \\
 &= \frac{n \times 26801.4 (\text{mA h})}{M_{\text{unit}} (\text{g})}
 \end{aligned}$$

Where, n is the number of transferred electrons in the redox reaction per repeating unit cell of the **COF**. F is the Faraday constant (96485 C mol⁻¹), and M_{unit} is the molecular weight of the repeating unit cell of the **COF**.

In the **COF** unit cell, the number of triazine units is 2, and the number of pyromellitic unit is 3. The molecular weight of the repeating triazine units (M_{Tz}) and pyromellitic unit (M_{Pm}) in the COF are 309.1266 and 214.0015, respectively (Scheme S5). The molecular weight of a unit cell is calculated to be-

$$M_{\text{unit}} = (2 \times M_{Tz}) + (3 \times M_{Pm}) = (2 \times 309.1266) + (3 \times 214.0015) = 1260.2577.$$

Now, C_t (mAh g^{-1}) will depend on the number of electrons (n) involved in the unit cell. The total number of maximum available electron in the unit cell is 12, considering of the fact that two electrons are involved in each pyromellitic unit ($3 \times 2 = 6$) and three electrons per triazine unit ($2 \times 3 = 6$). In the Table S3, theoretical specific capacity, C_t (mAh g^{-1}) calculation has been mentioned.

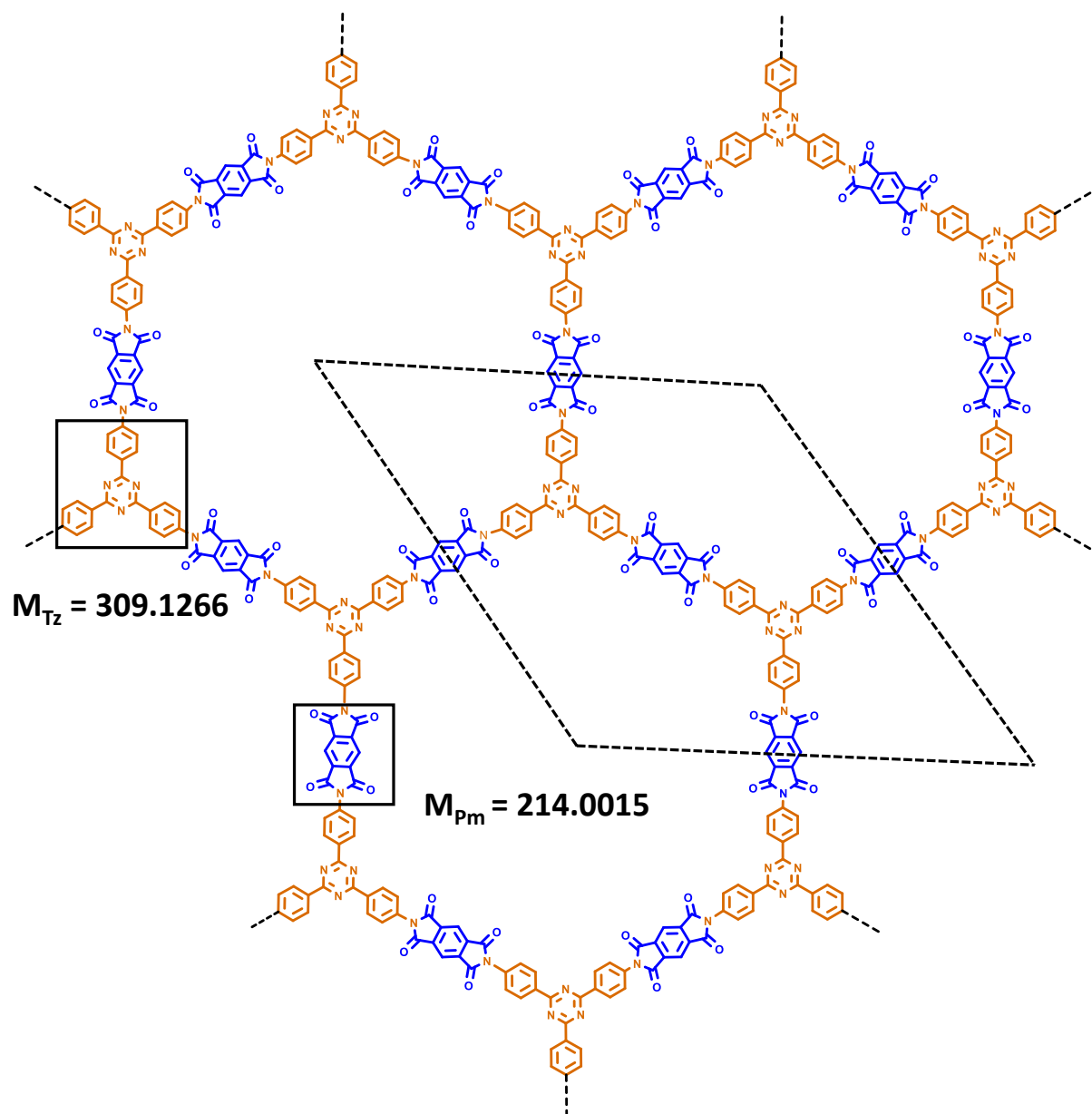


Figure S14. Chemical structure of COF. The unit cell is indicated by the dotted box.

Table S3. Calculation of theoretical specific capacity, C_t (mAh g^{-1}) with the variable number of electrons involved in the unit cell of the **COF**.

No of electrons	Unit involved	C_t (mAh g^{-1})
6	All 6 'O' center (pyromellitic)	127.6
6	All 6 'N' center (triazine)	127.6
7	6 'O' center (pyromellitic) + 1 'N' center (triazine)	148.8
8	6 'O' center (pyromellitic) + 2 'N' center (triazine)	170.1
9	6 'O' center (pyromellitic) + 3 'N' center (triazine)	191.4
10	6 'O' center (pyromellitic) + 4 'N' center (triazine)	212.7
11	6 'O' center (pyromellitic) + 5 'N' center (triazine)	233.9
12	6 'O' center (pyromellitic) + 6 'N' center (triazine)	255.2

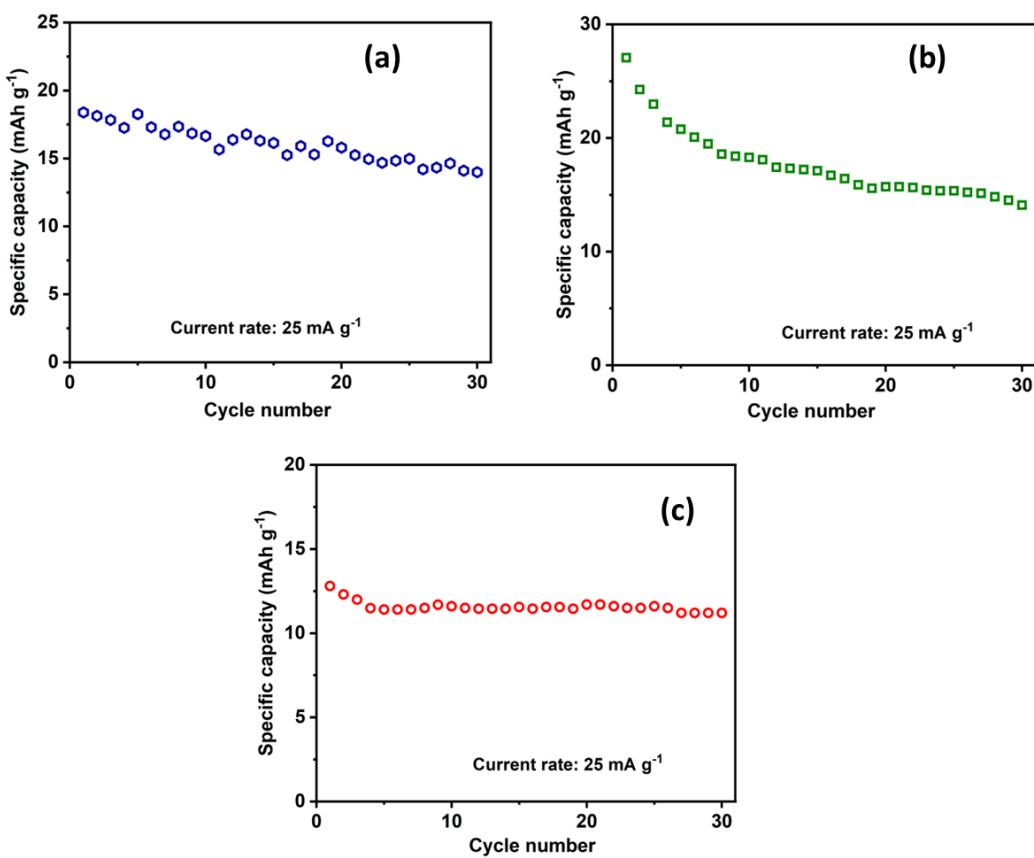


Figure S15. Cycling performance of (a) TAP TZ, (b) PMDA, and (c) MWCNT-NH₂ at 25 mA g^{-1} current density at 1.3-3.5 V voltage window.

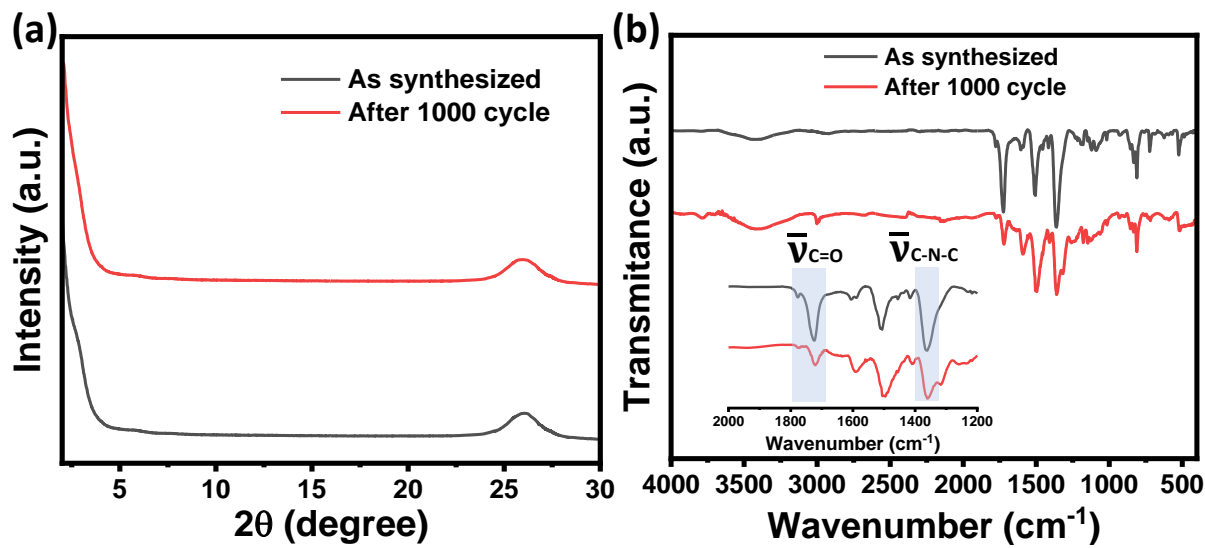


Figure S16. (a) PXRD patterns and (b) FTIR spectra of **COF@CNT-50** electrode before and after 1000 cycles of charge-discharge process. Inset data demonstrates the retention of the main IR stretching frequencies (-C=O and -C-N-C-) even after 1000 cycles.

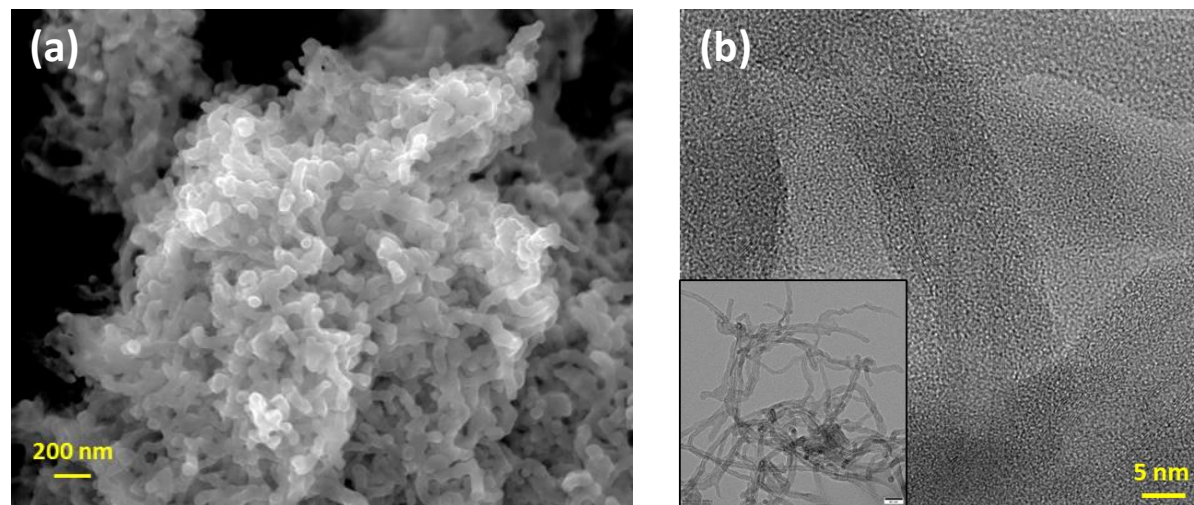


Figure S17. (a) FESEM and (b) HRTEM image of **COF@CNT-50** electrode after 1000 cycles of charge-discharge process.

Table S4. Electrochemical performance comparison of **COF@CNT-50** with organic polymer based cathodes for SIB.

Material	Redox active group	Potential window (V)	Maximum capacity (mAhg ⁻¹)	Capacity retention	Reference
TQBQ-COF	Carbonyl and pyrazine	1.0-3.8	452 at 0.02 A g ⁻¹	96% after 1,000 cycles at 1.0 A g ⁻¹	Nat Commun, 2020 , 11, 178
BPOE	Triazine	1.3-4.1	230 at 0.01 A g ⁻¹	80% after 40 cycles at 0.1 A g ⁻¹	Nat Commun, 2013 , 4, 1485
DAPT-TFP-CPF	Carbonyl	0.8-3.2	240 at 0.1 A g ⁻¹	~81% after 1,000 cycles 1.0 A g ⁻¹	J. Phys. Chem. Lett., 2018 , 9, 3205-3211
Aza-COF	Phenazine	0.01-3.0	545 at 0.1 C	~87% after 500 cycles at 5C	ACS Appl. Mater. Interfaces, 2021 , 13, 13, 15083-15091
S@TAPT-COFs hybrid	Carbonyl and triazine	1.5-3.2	109 at 0.1 A g ⁻¹	63% after 2000 cycles at 2.0 A g ⁻¹	Chem. Eng. J., 2023 , 453, 139607
NDI-TFP polymer	Carbonyl	1.3-3.3	90 at 0.05 mA g ⁻¹	~84% after 100 cycles at 0.3 A g ⁻¹	ACS Appl. Energy Mater., 2020 , 3, 11300-11306
CON-16	Triazine and thiophene	0.01-2.5	220 at 0.1 A g ⁻¹	~23% after 100 cycles at 0.3 A g ⁻¹	ACS Appl. Mater. Interfaces, 2018 , 10, 32102-32111
PICOF-1	Carbonyl	0.01-3.0	230 at 0.1 C	35% after 175 cycles at 0.3 C	Macromol. Rapid Commun., 2023 , 44, 2200782
COF@CNT-50	Carbonyl and triazine	1.3-3.5	164 at 0.025 A g⁻¹	69% after 1000 cycle 0.5 A g⁻¹	Our report

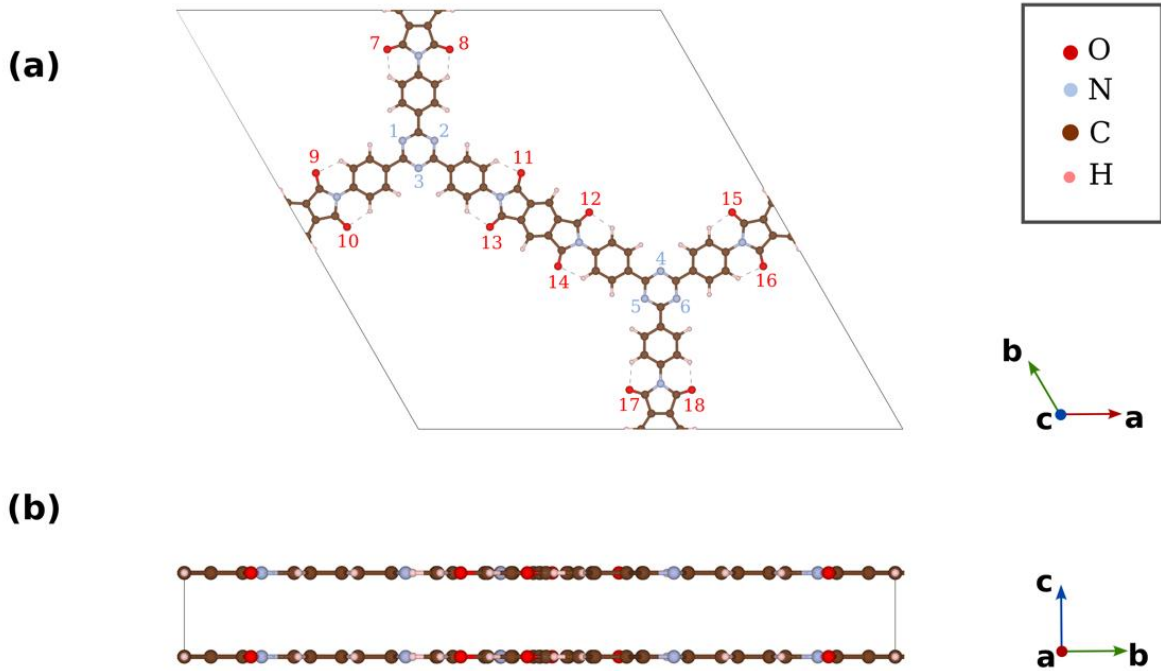


Figure S18. (a) Unit cell of the **COF** as obtained from PXRD, considered for the DFT calculations. All the possible Na-binding sites in the unit cell are numbered (1-18). The numbers in gray (1-6) indicate Na-binding sites adjacent to triazine C=N units, while numbers in red (7-18) indicate binding sites adjacent to the pyromellitic C=O units. (b) Side view of the unit cell shown in (a).

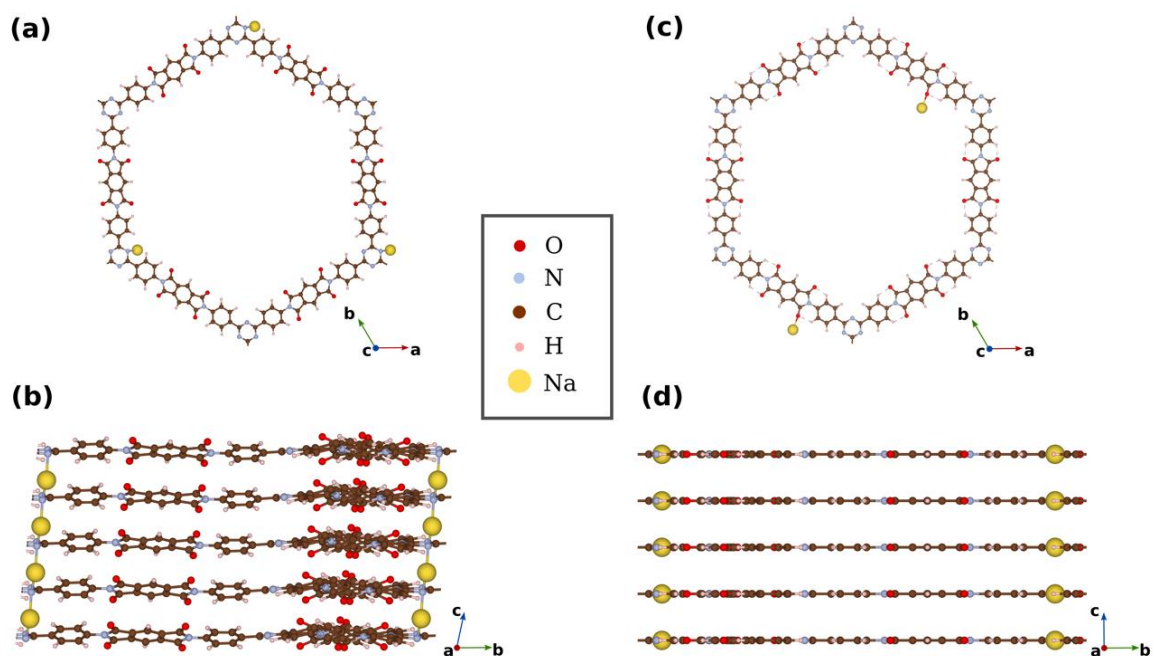


Figure S19. (a) Top view of the **COF** when the first Na^+ binds to the triazine C=N unit and

(c) binds to the pyromellitic C=O unit. (b, d) Side views of the structures in panels a and c, respectively, displaying 5 repeating units, indicating the (non-)planarity of each **COF** layer.

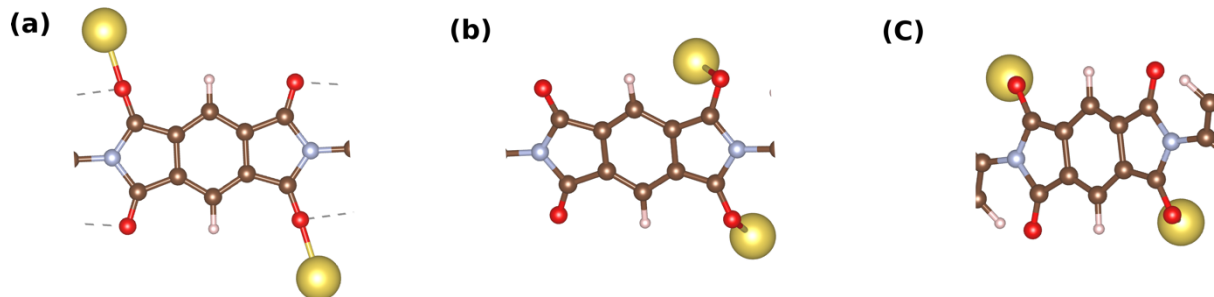


Figure S20. (a) Diagonal arrangement of Na^+ in the pyromellitic unit of a planar **COF**. (b) Adjacent arrangement and (c) distorted diagonal arrangement of Na^+ in the pyromellitic unit of non-planar **COF**.

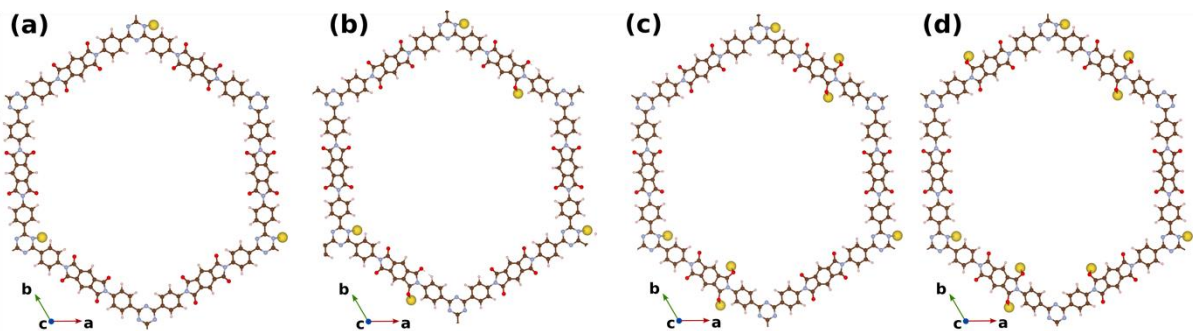


Figure S21. (a)-(d) Top view of the relaxed sodiated **COF** rings with 1- 4 Na^+ per unit cell, respectively.

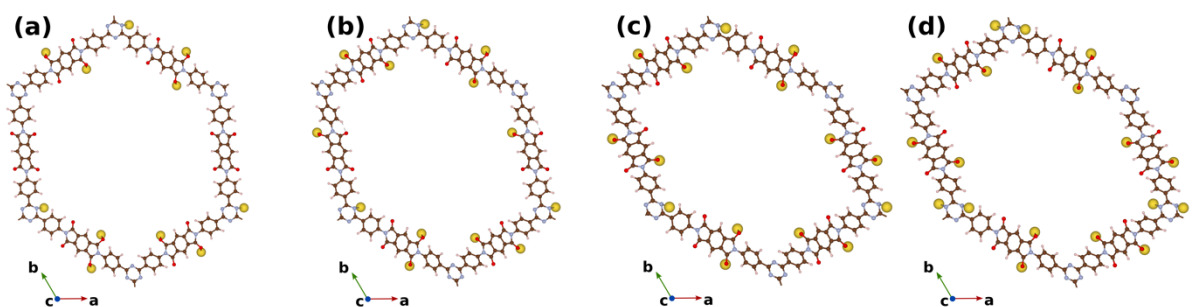


Figure S22. (a)-(d) Top view of the relaxed sodiated **COF** rings with 5 – 8 Na^+ per unit cell, respectively.

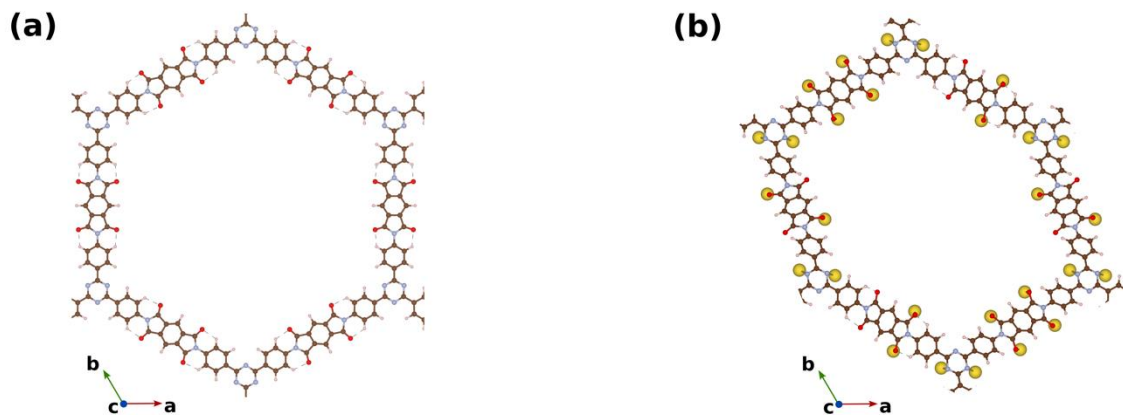


Figure S23. (a) Top view of the relaxed Na_0COF , and (b) Na_{12}COF rings, which are used as the reference states for the pseudo-binary convex hull.

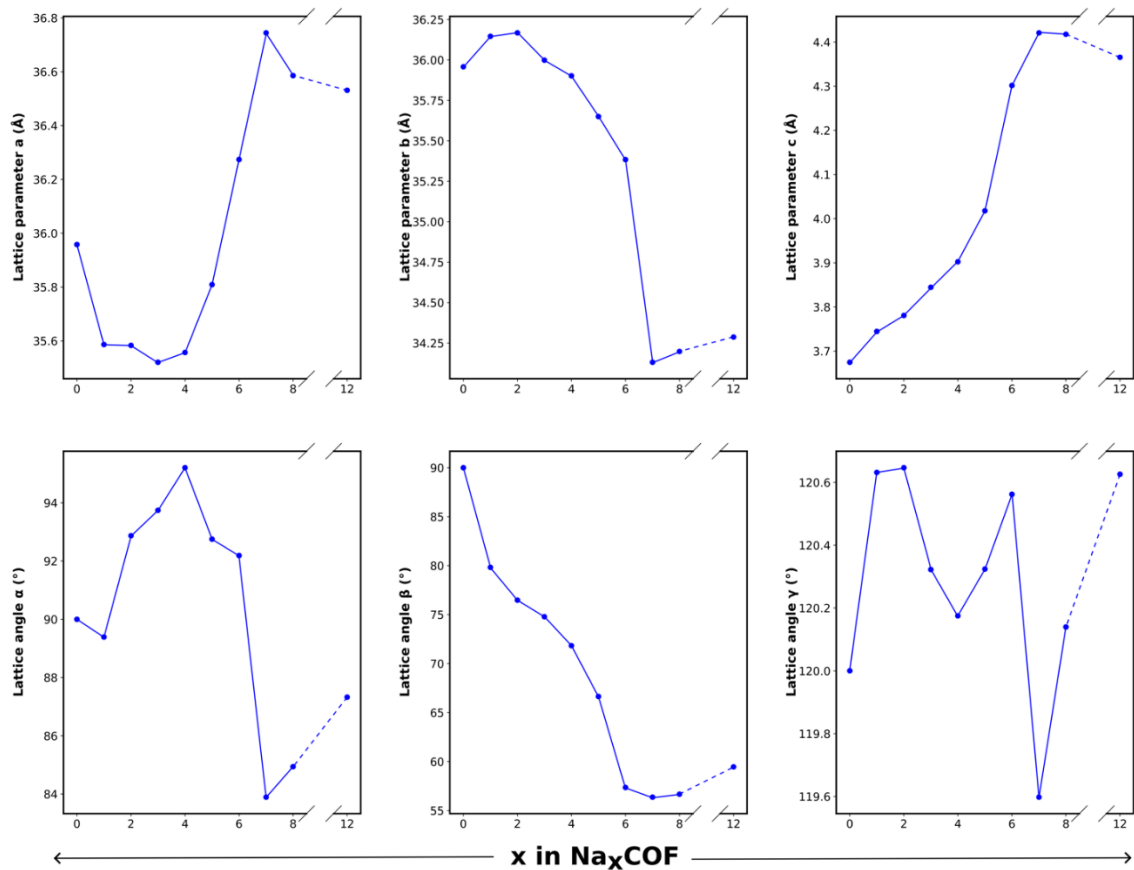


Figure S24. Variation in the lattice parameters and lattice angles of the COF unit cell (as shown in Figure S18) during sodiation.

Reference:

1. Halder, A.; Kandambeth, S.; Biswal, B. P.; Kaur, G.; Roy, N. C.; Addicoat, M.; Salunke, J. K.; Banerjee, S.; Vanka, K.; Heine, T.; Verma, S.; Banerjee, R., Decoding the Morphological Diversity in Two Dimensional Crystalline Porous Polymers by Core Planarity Modulation. *Angew. Chem., Int. Ed.* **2016**, *55* (27), 7806-7810.
2. Dey, A.; Chakraborty, S.; Singh, A.; Rahimi, F. A.; Biswas, S.; Mandal, T.; Maji, T. K., Microwave-assisted Fast Synthesis of a Donor-Acceptor Covalent Organic Framework towards Photooxidative Amidation Catalysis. *Angew. Chem., Int. Ed.* **2024**, *n/a* (n/a), e202403093.
3. Auras, F.; Ascherl, L.; Hakimioun, A. H.; Margraf, J. T.; Hanusch, F. C.; Reuter, S.; Bessinger, D.; Döblinger, M.; Hettstedt, C.; Karaghiosoff, K.; Herbert, S.; Knochel, P.; Clark, T.; Bein, T., Synchronized Offset Stacking: A Concept for Growing Large-Domain and Highly Crystalline 2D Covalent Organic Frameworks. *J. Am. Chem. Soc.* **2016**, *138* (51), 16703-16710.
4. Das, P.; Roeser, J.; Thomas, A., Solar Light Driven H₂O₂ Production and Selective Oxidations Using a Covalent Organic Framework Photocatalyst Prepared by a Multicomponent Reaction. *Angew. Chem., Int. Ed.* **2023**, *62* (29), e202304349.
5. Stähler, C.; Grunenberg, L.; Terban, M. W.; Browne, W. R.; Doellerer, D.; Kathan, M.; Etter, M.; Lotsch, B. V.; Feringa, B. L.; Krause, S., Light-driven molecular motors embedded in covalent organic frameworks. *Chem. Sci.* **2022**, *13* (28), 8253-8264.
6. Biswas, S.; Dey, A.; Rahimi, F. A.; Barman, S.; Maji, T. K., Metal-Free Highly Stable and Crystalline Covalent Organic Nanosheet for Visible-Light-Driven Selective Solar Fuel Production in Aqueous Medium. *ACS Catal.* **2023**, *13* (9), 5926-5937.
7. Kresse, G.; Hafner, J., *Ab initio* molecular dynamics for open-shell transition metals. *Phys. Rev. B* **1993**, *48* (17), 13115-13118.
8. Kresse, G.; Furthmüller, J., Efficient iterative schemes for *ab initio* total-energy calculations using a plane-wave basis set. *Phys. Rev. B* **1996**, *54* (16), 11169-11186.
9. Kresse, G.; Joubert, D., From ultrasoft pseudopotentials to the projector augmented-wave method. *Phys. Rev. B* **1999**, *59* (3), 1758-1775.
10. Sun, J.; Ruzsinszky, A.; Perdew, J. P., Strongly Constrained and Appropriately Normed Semilocal Density Functional. *Phys. Rev. Lett.* **2015**, *115* (3), 036402.
11. Ong, S. P.; Richards, W. D.; Jain, A.; Hautier, G.; Kocher, M.; Cholia, S.; Gunter, D.; Chevrier, V. L.; Persson, K. A.; Ceder, G., Python Materials Genomics (pymatgen): A

robust, open-source python library for materials analysis. *Comput. Mater. Sci.* **2013**, *68*, 314-319.

12. Ewald, P. P., Die Berechnung optischer und elektrostatischer Gitterpotentiale. *Ann. Phys.* **1921**, *369* (3), 253-287.